AGU PUBLICATIONS

JGR

Journal of Geophysical Research: Solid Earth

RESEARCH ARTICLE
10.1002/2015JB012210

Key Points:
- Frequency dependence of microseism sources between 0.325 and 0.725 Hz
- Transition from R_g to L_g waves with increasing frequency
- Generation of secondary microseisms by local wind sea in higher-frequency bands

Supporting Information:
- Supporting Information S1
- Figure S1
- Figure S2
- Figure S3
- Figure S4
- Figure S5

Correspondence to:
M. Gal,
martin.gal@utas.edu.au

Citation:
Gal, M., A. M. Reading, S. P. Ellingsen, L. Gualtieri, K. D. Koper, R. Burlacu, H. Tkalčić, and M. A. Hemer (2015), The frequency dependence and locations of short-period microseisms generated in the Southern Ocean and West Pacific, *J. Geophys. Res. Solid Earth*, *120*, 5764–5781, doi:10.1002/2015JB012210.

Received 15 MAY 2015
Accepted 3 AUG 2015
Accepted article online 6 AUG 2015
Published online 28 AUG 2015

The frequency dependence and locations of short-period microseisms generated in the Southern Ocean and West Pacific

M. Gal[1], A. M. Reading[1], S. P. Ellingsen[2], L. Gualtieri[3], K. D. Koper[4], R. Burlacu[4], H. Tkalčić[5], and M. A. Hemer[6]

[1]School of Physical Sciences (Earth Sciences) and CODES Centre of Excellence in Ore Deposits, University of Tasmania, Hobart, Tasmania, Australia, [2]School of Physical Sciences (Mathematics and Physics), University of Tasmania, Hobart, Tasmania, Australia, [3]Lamont-Doherty Earth Observatory, Columbia University, Palisades, New York, USA, [4]Department of Geology and Geophysics, University of Utah, Salt Lake City, Utah, USA, [5]Research School of Earth Sciences, Australian National University, Canberra, ACT, Australia, [6]CSIRO Oceans and Atmosphere Flagship, Hobart, Tasmania, Australia

Abstract The origin of the microseismic wavefield is associated with deep ocean and coastal regions where, under certain conditions, ocean waves can excite seismic waves that propagate as surface and body waves. Given that the characteristics of seismic signals generally vary with frequency, here we explore the frequency- and azimuth-dependent properties of microseisms recorded at a medium aperture (25 km) array in Australia. We examine the frequency-dependent properties of the wavefield, and its temporal variation, over two decades (1991–2012), with a focus on relatively high-frequency microseisms (0.325–0.725 Hz) recorded at the Warramunga Array, which has good slowness resolution capabilities in this frequency range. The analysis is carried out using the incoherently averaged signal Capon beamforming, which gives robust estimates of slowness and back azimuth and is able to resolve multiple wave arrivals within a single time window. For surface waves, we find that fundamental mode Rayleigh waves (R_g) dominate for lower frequencies ($<$0.55 Hz) while higher frequencies ($>$0.55 Hz) show a transition to higher mode surface waves (L_g). For body waves, source locations are identified in deep ocean regions for lower frequencies and in shallow waters for higher frequencies. We further examine the association between surface wave arrivals and a WAVEWATCH III ocean wave hindcast. Correlations with the ocean wave hindcast show that secondary microseisms in the lower-frequency band are generated mainly by ocean swell, while higher-frequency bands are generated by the wind sea, i.e., local wind conditions.

1. Introduction

Ambient seismic noise is the continuous background energy that is present in seismometer recordings. In the frequency range of 0.05–2 Hz, these microseisms have long been linked to ocean wave processes [e.g., *Wiechert*, 1904; *Gutenberg*, 1936; *Deacon*, 1947; *Traer et al.*, 2012]. The frequency spectrum of microseisms displays two peaks, around 0.07 Hz and 0.14 Hz, named the primary and secondary microseisms, respectively [*Friedrich et al.*, 1998; *Stutzmann et al.*, 2000; *Berger et al.*, 2004]. The primary microseisms are generated where pressure fluctuations from ocean waves interact with the ocean floor [*Hasselmann*, 1963; *Ardhuin et al.*, 2015]. For secondary microseisms, the underlying theory was first proposed by *Longuet-Higgins* [1950] and later extended by *Hasselmann* [1963]. The interaction of two opposing ocean wave trains with approximately the same wave number can generate pressure fluctuations that propagate unattenuated to the ocean bottom to excite seismic waves. Microseisms therefore carry information on the ocean state and the Earth structure between source and receiver.

The primary microseisms (PMs) are composed of Love and Rayleigh waves that are generated close to coastal areas [*Nishida et al.*, 2008]. The frequency of the PM ambient noise field is similar to the frequency of the ocean waves; hence, it carries information on near-shoreline ocean wave dynamics [*Aster et al.*, 2010]. For secondary microseisms (SMs), most of the energy is present in the form of Rayleigh waves [*Lacoss et al.*, 1969] and has been observed to have an origin close to coastal areas [*Bromirski et al.*, 2013], although SM energy generated in the deep ocean might also be observed on land [e.g., *Beucler et al.*, 2015].

A number of studies have focused on locating the source regions of SM Rayleigh wave energy with seismic arrays [*Cessaro*, 1994; *Friedrich et al.*, 1998; *Essen*, 2003; *Chevrot et al.*, 2007; *Kedar et al.*, 2008; *Koper et al.*, 2009;

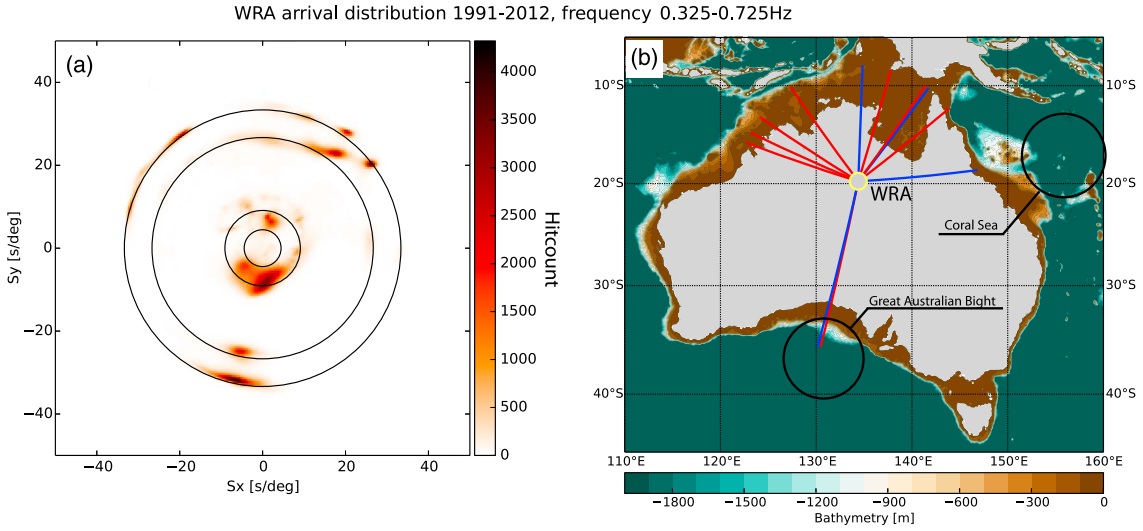

Figure 1. (a) Two-dimensional hit count histogram on a north-south (S_y) and east-west (S_x) slowness grid. This was derived using every 1 h segment of WRA data for the whole frequency range and time period of study using the IAS Capon algorithm. The outer circles are drawn at values of 30 s/deg and 26.5 s/deg corresponding to R_g and L_g slownesses. The inner circles are drawn at 9.1 s/deg and 4.5 s/deg and represent the boundaries for unbiased *P* wave backprojection (25°–98°). (b) The back azimuth of regional surface wave maxima extracted from Figure 1a and displayed on the continent of Australia centered on WRA (red: R_g Rayleigh waves, blue: L_g guided shear waves). The length of the displayed raypaths is not significant, and the exact source location is discussed in the text.

Behr et al., 2013; *Reading et al.*, 2014]. It was found that SM generation regions remain relatively constant over the period of a few days [*Schulte-Pelkum et al.*, 2004; *Chevrot et al.*, 2007] and show correlations with storm activity [*Schulte-Pelkum et al.*, 2004]. Coastal reflections [*Ardhuin and Roland*, 2012] and bathymetry effects [*Longuet-Higgins*, 1950; *Kedar et al.*, 2008] were shown to be important factors for an improved understanding of microseisms recorded by on-land seismic stations.

The excitation of SM body waves is mainly driven by strong ocean storms and primarily observed in deep ocean regions [*Gerstoft et al.*, 2008]. Slowness estimation with a seismic array enables the inference of body wave source location through backprojection. Such teleseismic raypaths also elicit information on the interior structure of the Earth [*Boué et al.*, 2013]. In our earlier study [*Reading et al.*, 2014], over a decade of continuous data (2000–2012) from the Warramunga Array (WRA) in central Australia were analyzed. The work was carried out in a single frequency band of 0.4–0.6 Hz and identified multiple surface wave arrivals surrounding Australia and three dominant *P* wave sources in the Southern Ocean and West Pacific for which the seasonal patterns were studied.

Here we analyze the frequency dependence of the microseismic wavefield in the frequency range of 0.325–0.725 Hz observed at WRA. We estimate its properties in eight distinct frequency bands, with a width of 0.05 Hz for each band, and include a detailed slowness-azimuth station correction (SASC) calibration. Although the frequency bands are narrow in the context of ocean-induced seismic ambient noise analysis in general, the frequency range corresponds to ocean swells or wind seas with periods between ~2.75 and 6.15 s. This allows the investigation of variations in SM generation for each frequency band. The analysis is further extended from that of *Reading et al.* [2014] by including an additional decade of data (1991–2000) and, importantly, interpreting multiple distinct microseism arrivals within a particular time window, as opposed to only the largest. We relate our seismic results to ocean site effects, ocean and wind properties, and include a brief analysis of seasonal variations.

2. Data and Methods

2.1. Overview of Data Used

We use data from the Warramunga Array (WRA), located in central Australia (Figure 1), from 1991 to 2012. The array is operated by the Australian National University as part of the International Monitoring System (IMS)

network and was originally deployed for the long-range detection of nuclear explosions. The multidecadal record from WRA has significant gaps of 4–5 months in the years 1997, 2006, and 2007; 8 months in the year 2009; and no data are available in the years 1998 and 1999. For all other years the data are complete.

2.2. Array Properties

WRA initially consisted of 20 short-period, vertical component stations deployed in an "L" shape with irregular interstation spacing of 2–3 km. In 1999, four three-component stations were added to the existing network (Figure S1a in the supporting information, figures are denoted with an "S"), and all stations were upgraded to broadband. The interstation spacing of WRA allows the accurate study of regional surface waves (0.3–1 Hz) and body waves (0.5–2 Hz) with respect to the array response (Figures S1c–S1e). WRA provides a multidecade set of continuous seismic data in a central position in Australia and is thus appropriate for the synoptic study of short-period microseism properties. In this study, we focus exclusively on the vertical component of the WRA sensors.

2.3. Array Calibration

It is well known that many small-to-middle-aperture seismic arrays exhibit a systematic bias in slowness and back azimuth estimates [e.g., *Manchee and Weichert*, 1968]. This bias can be mainly explained by bending/refraction of seismic waves at the boundary of geological structures beneath the array, for instance, Moho topography [*Jacobeit et al*., 2013]. With independent knowledge of the origin of the seismic signal, the bias can be accounted for by calculating mislocation vectors for the given array and the application of the resulting slowness-azimuth station corrections (SASCs). Here we perform mislocation vector analysis [*Bokelmann*, 1995; *Bondár et al*., 1999; *Schweitzer*, 2001] for WRA to ensure accurate slowness estimates for observed microseisms. For this purpose we consider earthquakes with a magnitude of 3.5 m_b or higher from the International Seismological Centre (ISC) catalog [*International Seismological Centre*, 2012] for the two full years of 2010–2011. To obtain suitable coverage for the southern Indian Ocean, which has lower seismicity than areas to the north, we analyze all earthquakes below the latitude of 30°S for the additional years 2001–2009. We consider only earthquakes located at distances farther than 25°. Body waves that are generated closer than 25° turn in the upper mantle and may lead to biased results owing to triplicated arrivals. We therefore make use of epicentral distances greater than 25° in the study of body wave microseisms, with an upper limit of 98°. From this list, all earthquakes with overlapping *P* arrivals from different back azimuths are excluded, leaving a total of 22,175 earthquakes.

The earthquake waveforms are extracted in 100 s lengths, where the *P* wave onset is positioned 50 s into the window. Each segment is tapered with a Hann window, and an implementation of the IAS Capon beamforming [*Gal et al*., 2014] is used to estimate slowness and back azimuth. The recovered back azimuths are compared to those expected for the ISC locations, while slowness values are compared to theoretically predicted values from the "ak135" model [*Kennett et al*., 1995]. The mislocation vectors are presented in Figure S1b, where a 0.5 s/deg grid spacing was used. To reduce statistical errors, we follow the methodology of *Bondár et al*. [1999] and compute the median for each slowness cell. Correction vectors are displayed if at least five earthquakes enter into the estimation, with the corresponding standard deviations of slowness below 1 s/deg and back azimuth below 0.3°. The slowness spectrum shows a good agreement with the results of *Bondár et al*. [1999] and highlights two potential back azimuths (~170° and ~330°), where corrections are significant. We do not see a systematic bias that would potentially point to a dipping geological layer [*Jacobeit et al*., 2013] below the array. The generated mislocation vectors are used to compute an interpolated vector field that extends corrections systematically to other slowness vectors. We take these corrections into account during backprojections of *P* waves.

2.4. Analysis Methods

For the years 1991–1999 we evaluate a 1 h segment every 3 h owing to limitations in data availability, while for the years 2000–2012 all available hours of data are analyzed. For the continuous data recorded prior to 2000 (short-period vertical, SHZ), we remove the instrument response. For data recorded after 31 December 2000 (broadband vertical, BHZ), the instrument response is flat over the analyzed frequency bands and response deconvolution is not needed. The beamforming algorithm averages over multiple narrowband slowness spectra, and its stability is ensured via diagonal loading of the cross-power spectral density. It has been shown that IAS Capon recovers slowness vectors accurately and is able to resolve multiple arrivals [*Gal et al*., 2014] in a given time window. The analysis is performed in eight frequency bands with

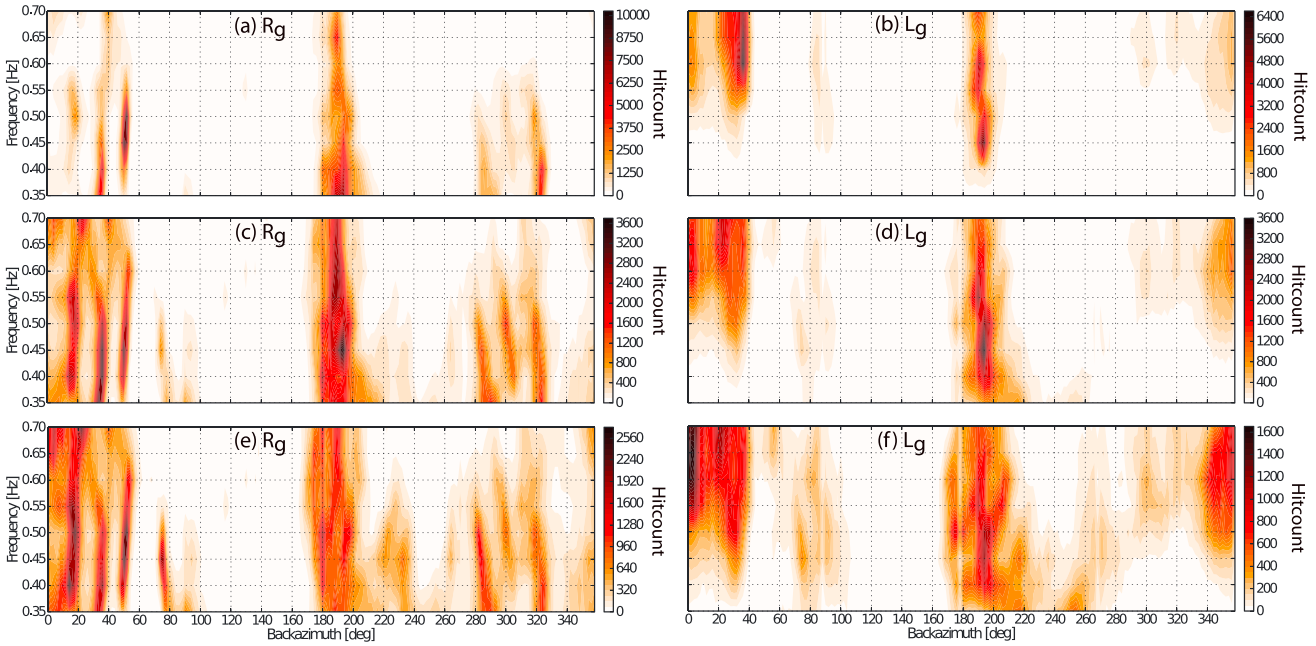

Figure 2. Representation of dominant (a) R_g and (b) L_g arrivals with respect to frequency. Weaker phases, namely, second and third strongest surface wave arrivals, for (c and e) R_g and (d and f) L_g with respect to frequency.

widths of 0.05 Hz in the range of 0.325 to 0.725 Hz. A 1 h record is divided into 35 time slices, with an overlap of 50%, and the Hann windowing function is applied to reduce spectral leakage. For each estimated slowness spectrum, up to 10 local maxima of surface and body waves within a ±50 s/deg slowness grid are extracted. For the arrivals associated with local maxima, we require the estimated power to be greater than 80% of the global maximum to avoid spurious or sidelobe effects. An example of a beamforming analysis combined with the extraction of maxima from the slowness domain is presented in Figure S2.

3. Results

3.1. Dominant Microseism Arrivals

Using the IAS Capon method, we identified ~6.9×10^6 arrivals over the period of 1991–2012. In the following section we focus on the strongest arrivals, i.e., those corresponding to the absolute maximum of beam power in a particular time window. We find an approximately equal number of surface (52%) and body waves (48%) for the dominant arrivals. We observe a slight resolution increase in surface and body wave slowness peaks after 1999, which we attribute to the upgrade of instruments and the deployment of four additional stations; however, the results before and after the station upgrades are very similar and can therefore be evaluated together.

3.1.1. Surface Waves

For surface waves, we find multiple spatially concentrated source regions and present the corresponding hit count plot in Figure 1a. The analysis reveals two separate phases with velocities around 3.3 km/s and 4.1 km/s, which can be associated with fundamental mode Rayleigh waves (R_g) and supercritical S waves trapped in the crustal waveguide (L_g). We have validated both phase velocities, R_g 3.3 ± 0.1 km/s and L_g 4.1 ± 0.2 km/s, by performing IAS Capon analysis on R_g and L_g coda from a local earthquake. By extracting the slownesses from the maxima of the hit count plot (Figure 1a), we generate raypaths oriented toward R_g and L_g source regions (Figure 1b). The result suggests the presence of favorable coastline conditions for the generation of short-period microseisms, i.e., reflectors of swell and wind sea. This can either be small islands, close to coastal regions, as supported by the three arrivals from the northeast (Figure 1b) or bays where a more coherent reflection of the ocean wave train over a larger area is likely. A summary of all eight frequency bands can be seen for R_g (Figure 2a) and L_g waves (Figure 2b). For lower frequencies (0.325–0.425 Hz) we find R_g waves only, while higher-frequency bands (>0.5 Hz) show a transition to L_g waves. The figure further shows

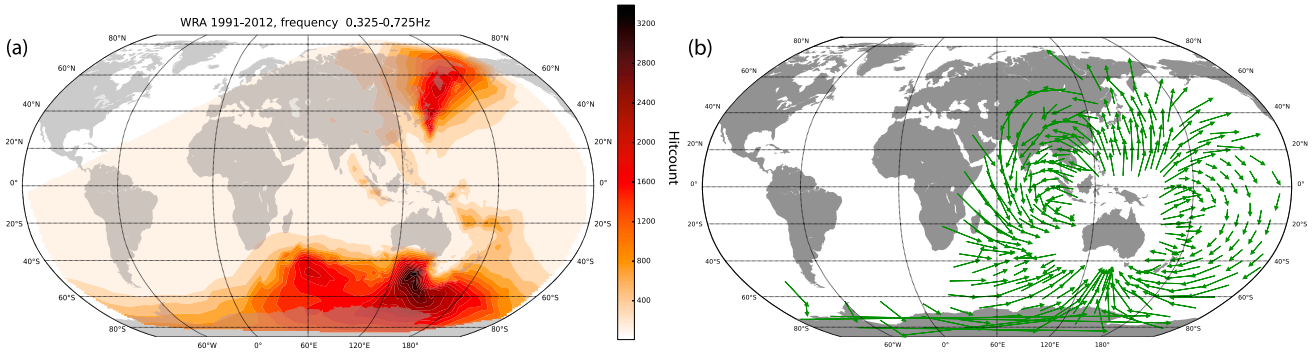

Figure 3. (a) Backprojection of dominant *P* wave arrivals for all eight frequency bands and the full study period with SASCs applied. Maxima are found in the southern Indian Ocean (south of Australia), the Kerguelen Plateau, and the east coast of Japan. (b) Backprojection of the mislocation vectors onto the world map to visualize their impact on the interpretation.

a frequency-dependent signal strength; i.e., different sources dominate for different frequency bands. Only minor changes in back azimuth occur that might be connected to bathymetry effects [*Kedar et al*., 2008; *Gualtieri et al*., 2013]. The only exception is an extended area of generation between the back azimuths of 180–220° in the low-frequency bands (0.375–0.525 Hz), which gradually shifts toward a lower back azimuth as frequency increases. We analyzed the azimuthal sensitivity of WRA due to its station geometry (Figures S3a and S3b) and did not find any bias toward the arrival directions of R_g and L_g waves.

3.1.2. Body Waves

Combining all eight frequency bands together, we obtain the *P* wave arrival hit count plot for the period of our study (Figure S4a). Only arrivals that are between the two circles, which correspond to slownesses (distances) of 9.1 s/deg (25°) and 4.45 s/deg (98°), are used for backprojection. We assume *P* wave propagation for the purpose of body wave backprojection as this has been used successfully for microseisms in higher-frequency range [*Zhang et al*., 2009] as in our study. A potential difficulty in the frequency-dependent analysis is created by earthquakes. While lower frequencies show a relatively earthquake-free hit count summary, higher frequencies are affected by earthquake arrivals. This is due to the spectral properties of the ambient wavefield, as lower frequencies show greater amplitudes than higher frequencies (for our range 0.325–0.725 Hz), while *P* arrivals from earthquakes tend to have larger SNR in the higher-frequency range. We do not attempt to discard time intervals that are affected by earthquakes, as these still provide information on weaker ambient noise signals.

To visualize areas with high earthquake potential, we analyzed over 10,000 earthquakes through a full year of the ISC bulletin [*International Seismological Centre*, 2012] (Figure S4b). After accounting for these, three distinct noise sources remain that match our earlier study [*Reading et al*., 2014]. We overlay the information on the figure with the mislocation vector results to indicate biased arrivals (Figure S4a). We backproject body wave arrivals as *P* arrivals with the mislocation vectors plotted to stress the importance of the array calibration (Figure 3). The *P* wave arrivals from the north correlate well with the east coast of Japan, arrivals from the south with the southern Indian Ocean (south of Australia) and arrivals from southwest with the Kerguelen Plateau. Although the east coast of Japan is a region of strong seismicity, we are confident that the observed body waves are generated by ocean waves (see also section 3.2.2). Without the SASCs, the Indian Ocean source would map more strongly on to the continent of Antarctica (assuming *P* and not *PP* propagation). This emphasizes the importance of applying the SASCs, which can be as large as 25°, i.e., ~2780 km. We also analyzed the azimuthal sensitivity of WRA for *P* waves (Figure S3c) averaged over all eight frequency bands and found our results to be robust.

The frequency-dependent analysis reveals that the maximum number of arrivals for the lowest-frequency band originate in the southern Indian Ocean (Figure 4a). The position of the peak shifts to the west for the second lowest-frequency band and then continues to shift, with increasing frequency, toward the Great Australian Bight (Figure 4a). For the *P* waves from the northern hemisphere, we find the source location in the lowest-frequency band to be in the area of the Kamchatka Peninsula, namely, north of the Sea of Okhotsk, shifting toward the east coast of Japan for the highest frequencies (Figure 4b). The shifting locations of the dominant *P* wave arrivals for different bands in the southern Indian Ocean and Japan region will be

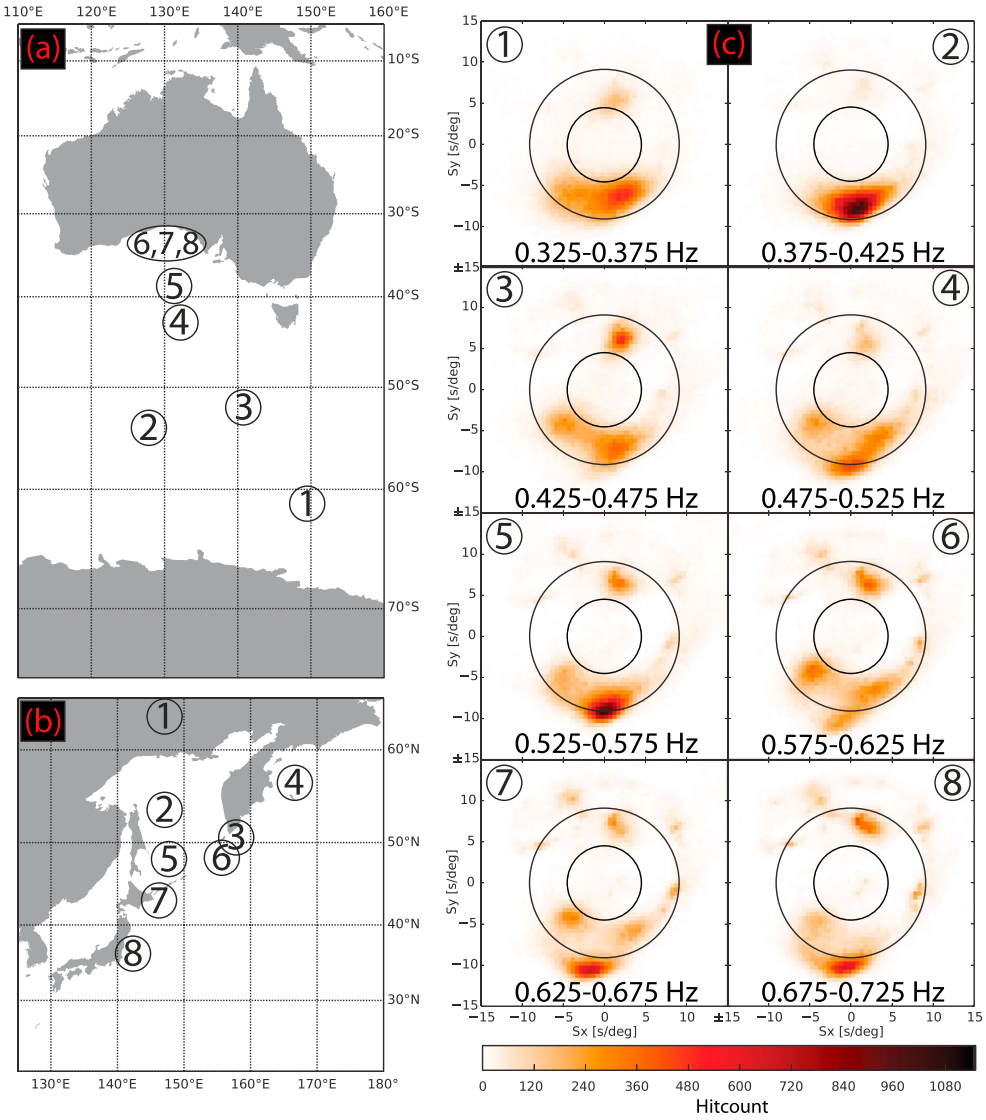

Figure 4. Maxima of dominant *P* wave arrivals for each frequency band with SASC applied. Arrivals for each frequency band from (a) south of Australia and (b) Sea of Okhotsk and Japan area. (c) Corresponding slowness plots for each frequency band. Analog to Figure 1a, the area between the two circles is used for *P* wave backprojection.

examined in the context of ocean site effects in section 4.1. The arrivals from the Kerguelen Plateau do not show significant shifts in location with frequency for bands 3–8 (bands 1 and 2 do not have local maxima in *P* wave arrivals at this location). The corresponding slowness spectra that were used for the backprojection are presented in Figure 4c. An increase in the hit count in earthquake arrivals with increasing frequency is observed, as described previously.

3.2. Weaker Microseism Arrivals

3.2.1. Surface Waves

We now focus on the analysis of weaker microseism arrivals that correspond to local (but not global) beam power maxima in slowness space. For every hour of processed data, we extract lower strength arrivals above a predefined threshold (those within 20% of absolute maxima). We then follow the procedure of section 3.1 and generate hit count plots in frequency-back azimuth space (Figures 2c–2f). The frequency-dependent analysis for the weaker arrivals is in good agreement with the main arrival analysis and shows new regions that generate surface waves. For low frequencies, we observe weak L_g arrivals from the south and west, which were not previously identified. For frequency bands 2–5 (0.375–0.575 Hz) we observe surface wave arrivals

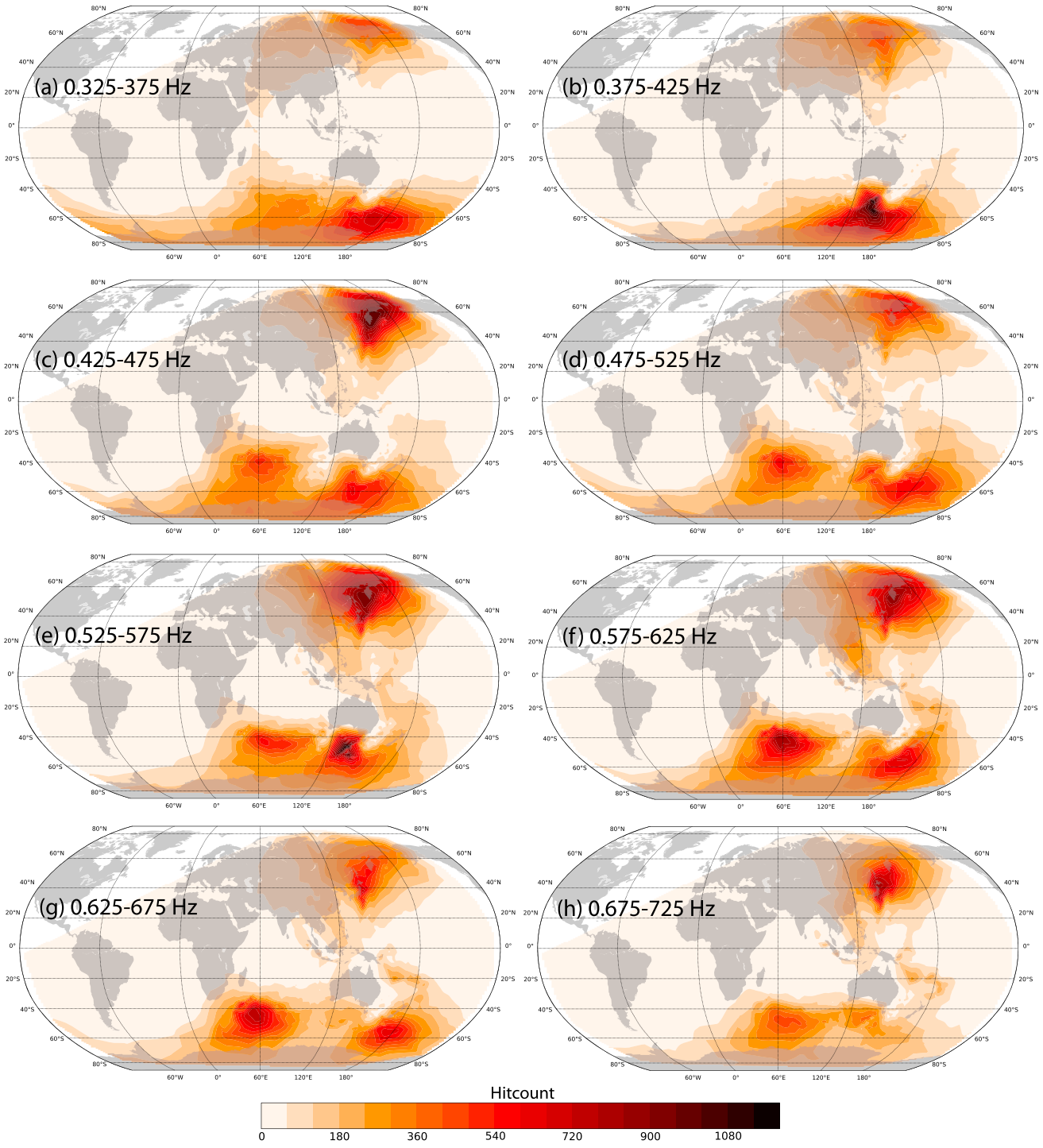

Figure 5. (a–h) A summary of dominant and weaker *P* wave arrivals combined for each frequency band and period of the study with SASCs applied. The addition of weaker arrivals allows for a more complete representation of *P* wave generation regions in each band.

from all directions except the southeastern region, which remains arrival free for all periods and frequencies of our study. For higher frequencies, R_g and L_g wave arrivals are primarily from the south and north.

The analysis of weaker signals reveals that spatially concentrated surface waves are active in a broader frequency range. Sources appear to slightly change back azimuth with frequency. Arrivals between 280 and 330° shift toward a lower back azimuth with increasing frequency, while sources between 30 and 55°

shift toward a higher back azimuth with increasing frequency. Possible reasons for the shift in frequency will be covered in the Discussion section. For dominant L_g arrivals, we observe a slight variability from the source region at 180–220°, and multiple arrivals do not reveal variations in source location. We find good agreement between R_g and L_g source locations, which favors the idea of an R_g-to-L_g conversion mechanism [*He et al*., 2008], except for the source region at back azimuths near 50° which displays weak L_g arrivals. R_g waves dominate the lower frequencies, and a possible conversion example can be seen around 35° where R_g arrivals are converted to L_g above 0.55 Hz.

3.2.2. Body Waves

For body waves associated with secondary beam power maxima, we find results similar to those from global slowness maxima, where most of the arrivals correspond to the Kamchatka region, Kerguelen Plateau, and southern Pacific Ocean (Figure S5). Earthquakes do not interfere in this analysis, as only weaker arrivals are plotted. This can be seen from the comparison between Figure S5a and Figures S5b and S5c, as areas with sharp contrasts that symbolize earthquake arrivals (Figure S4b) are eliminated or minimally present for secondary beam power maxima. New arrival patterns appear that correspond well with the east coasts of Japan, Taiwan, and the Philippines. The weaker arrivals, which show no bias due to earthquakes, give us confidence that the observed body waves are generated by ocean wave interactions. For the northeast region, the Coral Sea correlates well with an increased arrival hit count region. An overview of backprojected *P* waves, combining dominant and weaker arrivals for all eight frequency bands, is shown in Figure 5.

4. Interpretation

4.1. Effect of Bathymetry

We relate our results to the bathymetry- and frequency-dependent amplitude coefficients for a half-space over a flat-Earth model [*Longuet-Higgins*, 1950] for the analysis of surface waves. The coefficients can be seen as an energy transfer function between the liquid and solid layers and are dependent on the depth of the ocean layer and the seismic wave frequency. The maximum of energy transfer occurs at depth and frequency combinations that can be associated with resonant behavior and differs between seismic wave phases (R_g, *P*, *S*…). For the analysis of *P* waves, we use the approach of *Gualtieri et al*. [2014], in which the amplitude coefficients are described by a plane wave decomposition and are in addition dependent on the distance between source and receiver. We compute amplitude coefficient maps for the case of surface and body arrivals and compare them with observations (sediment layers are not accounted for in both cases).

For surface waves, we display the frequency bands 1 (Figure 6a) and 8 (Figure 6b) as a sum of all years for combined R_g and L_g arrivals and their corresponding fundamental coefficient maps for 0.35 Hz and 0.7 Hz (Figures 6c and 6d). At 0.35 Hz, the regions with high-amplitude coefficients show some surface wave arrivals but cannot explain all arrivals. For spatially concentrated sources in the north, the amplitude map does not explain the strong directional behavior found in the data. For higher frequencies, we find a reduction of high-amplitude regions that is well correlated with the observed seismic arrivals for these back azimuths. Owing to the higher frequency, areas with favorable amplitude coefficients move into shallower water, yet they still cannot explain the sources from the north and south. We see a reduction in the number of arrivals from distant coastlines. The spatial concentration of surface arrivals cannot be explained by bathymetry effects alone in either case, and possible reasons for this will be discussed in section 5.

For *P* waves, we generate amplitude coefficient maps following the work of *Gualtieri et al*. [2014] for the region south of Australia (Figure 7a) and the Kamchatka/Japan region (Figure 7b), for all eight frequency bands. For the region south of Australia we find the maxima of *P* wave arrivals in the first four bands to be in close vicinity to favorable amplitude coefficient regions. For higher-frequency bands, the maxima of arrivals are found in more shallow water and are less correlated than for lower frequencies. For the northern hemisphere, we see good correlations in bands 2, 4, 5, and 6. Bands 7 and 8 are again associated with shallow water/coastlines and do not show strong correlations with amplitude coefficients. Band 1 shows the maximum of *P* arrivals to be located on land north of the Sea of Okhotsk. A possible explanation is that these are actually *PP* arrivals from one of the well-known microseism source regions in the North Atlantic [*Kedar et al*., 2008]. For the Kerguelen Plateau, the source locations are found within a few degrees of the Kerguelen Islands for bands 3–8 (Figures 5d–5h).

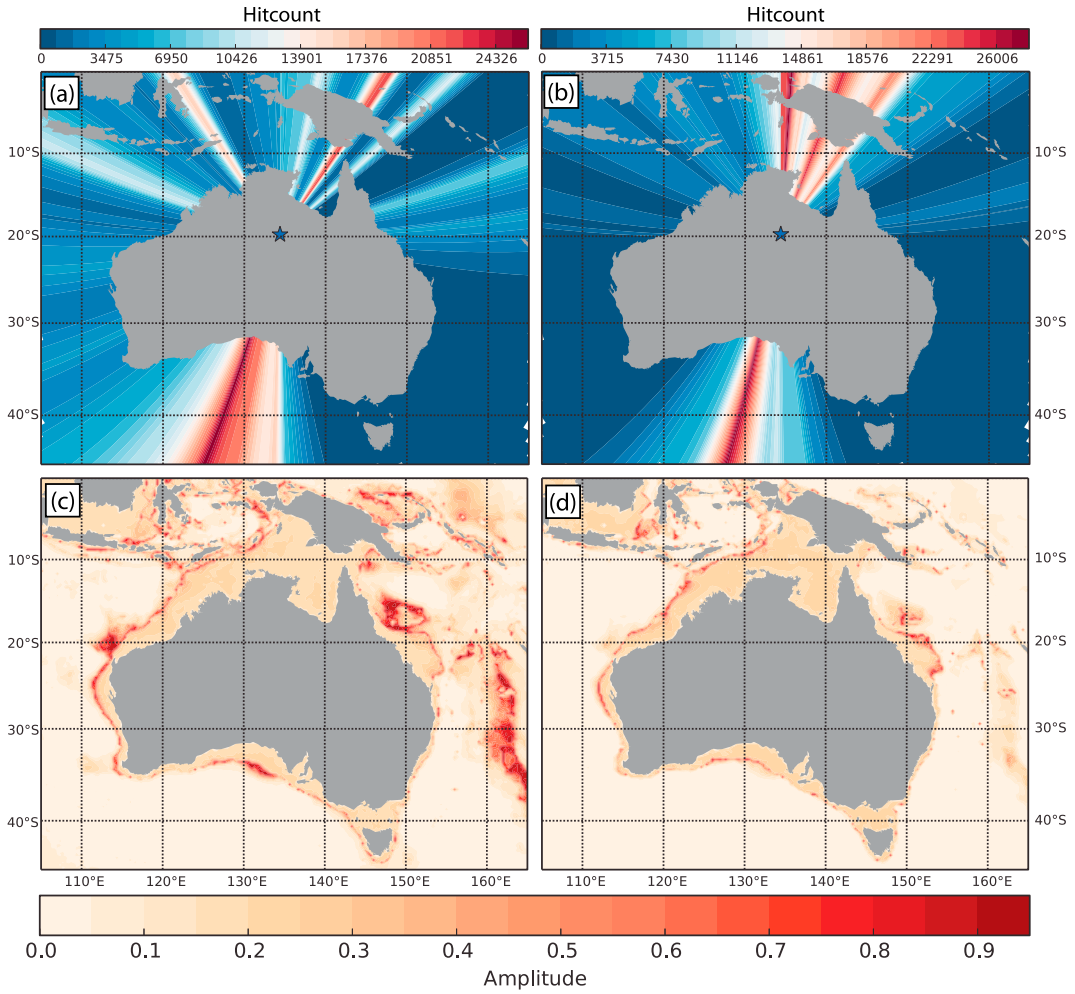

Figure 6. (a) Surface wave arrivals, R_g and L_g, for frequency band 1. The estimated arrivals are discretized into 2° bins and displayed on their respective raypaths. We have used up to five arrivals per hour for the whole period of the study. (b) R_g and L_g arrivals for frequency band 8. The fundamental amplitude coefficient derived from *Longuet-Higgins* [1950] is displayed for the appropriate frequency: (c) band 1 and (d) band 8.

The maximal *P* wave arrivals in the low-frequency bands are located in areas with favorable amplitude coefficients, but not all areas with high-amplitude coefficients show *P* wave arrivals; hence, ocean site effects alone cannot explain the observed distribution of *P* wave arrivals. We expect the inhomogeneous swell distribution and spatial reflector distribution to be the main causes. The majority of storms follow a certain spatial pattern and generate similar swells that can be reflected by coastlines. Ocean regions close to coastlines that lie in the main storm tracks therefore generate better conditions for SM generation [*Ardhuin and Roland*, 2012]. For higher-frequency bands, we observe a decrease in the influence of ocean site effects on the *P* wave generation regions, and coastline reflection seems to play a more important role. It should be further mentioned that coastline reflection is not the only contribution for favorable SM generation regions—we detect *P* wave arrivals east from the Kerguelen Islands, which suggests that ocean swells bend around the islands to form areas with opposing wave trains.

4.2. Correlations With Ocean and Wind Dynamics

Our multidecadal short-period microseism analysis allows us to search for general correlations between the seismic arrivals and an ocean wave hindcast. The hindcast was performed using the WAVEWATCH III, v4.08 software, and was forced hourly with Climate Forecast System Reanalysis surface winds and sea ice variations [*Durrant et al.*, 2013a, 2013b]. The wave spectra are discretized over 29 exponentially spaced frequencies

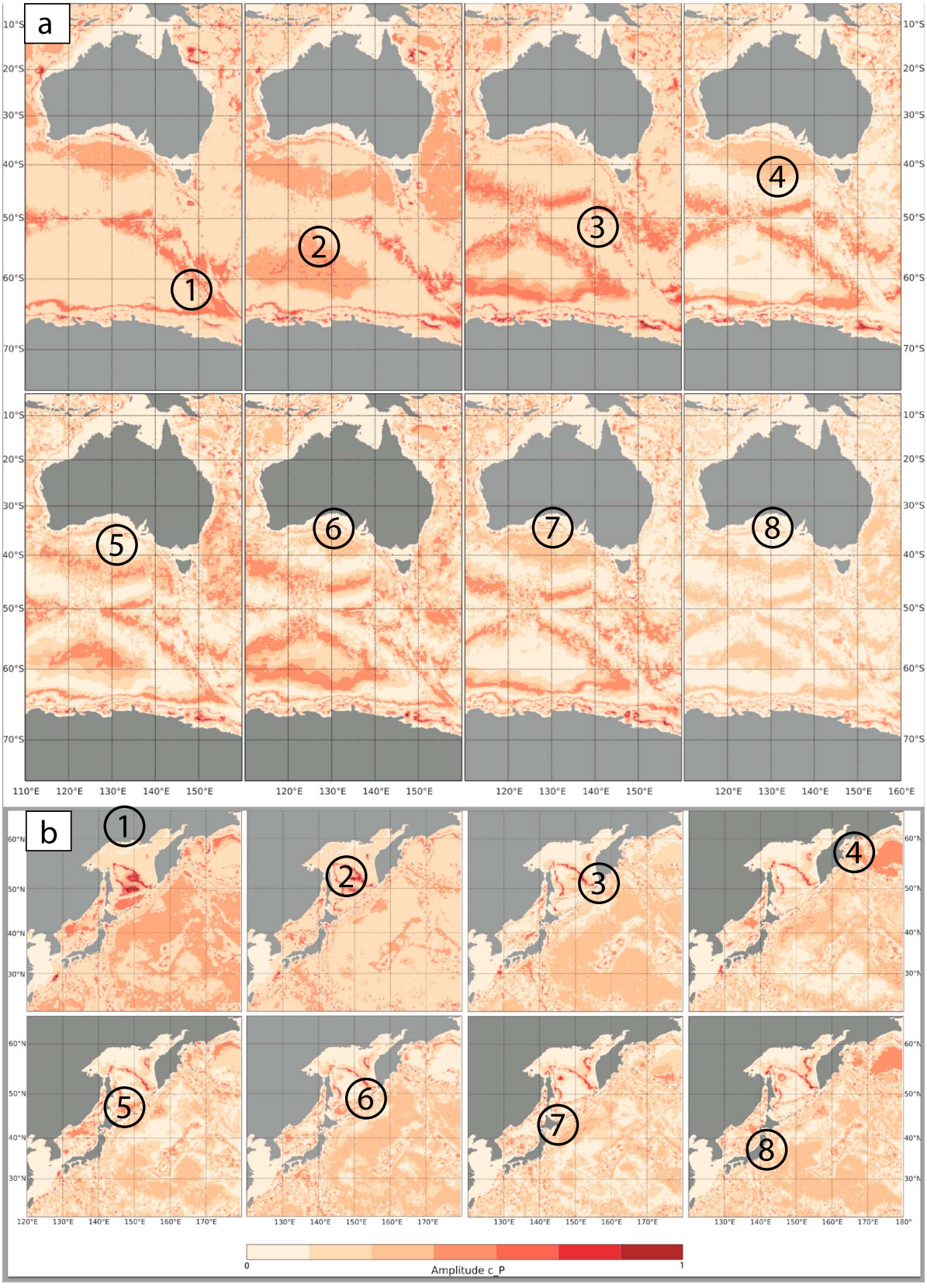

Figure 7. Amplitude coefficients for all eight frequency bands for (a) south of Australia and (b) Kamchatka/Sea of Okhotsk/Japan region. The maximum of *P* wave arrivals is marked with a black circle for each band (SASC applied). The amplitude coefficient maps are generated by averaging over the whole width of the frequency band.

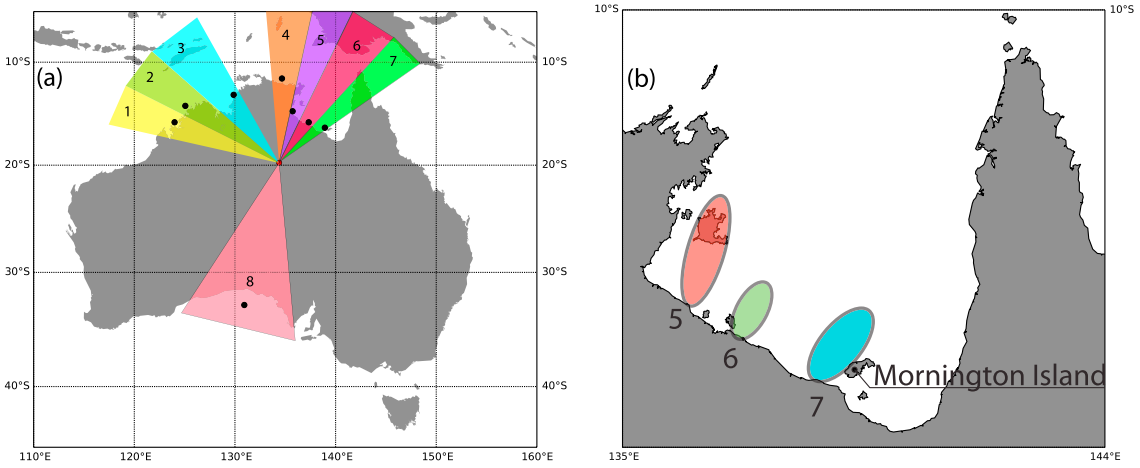

Figure 8. (a) Discretization of back azimuths for the comparison with ocean and wind dynamics. A grid location that coincides with the maximum of surface wave arrivals is selected in each sector to represent the local ocean and wind properties. (b) Possible generation locations for R_g waves in the northeast basin of Australia.

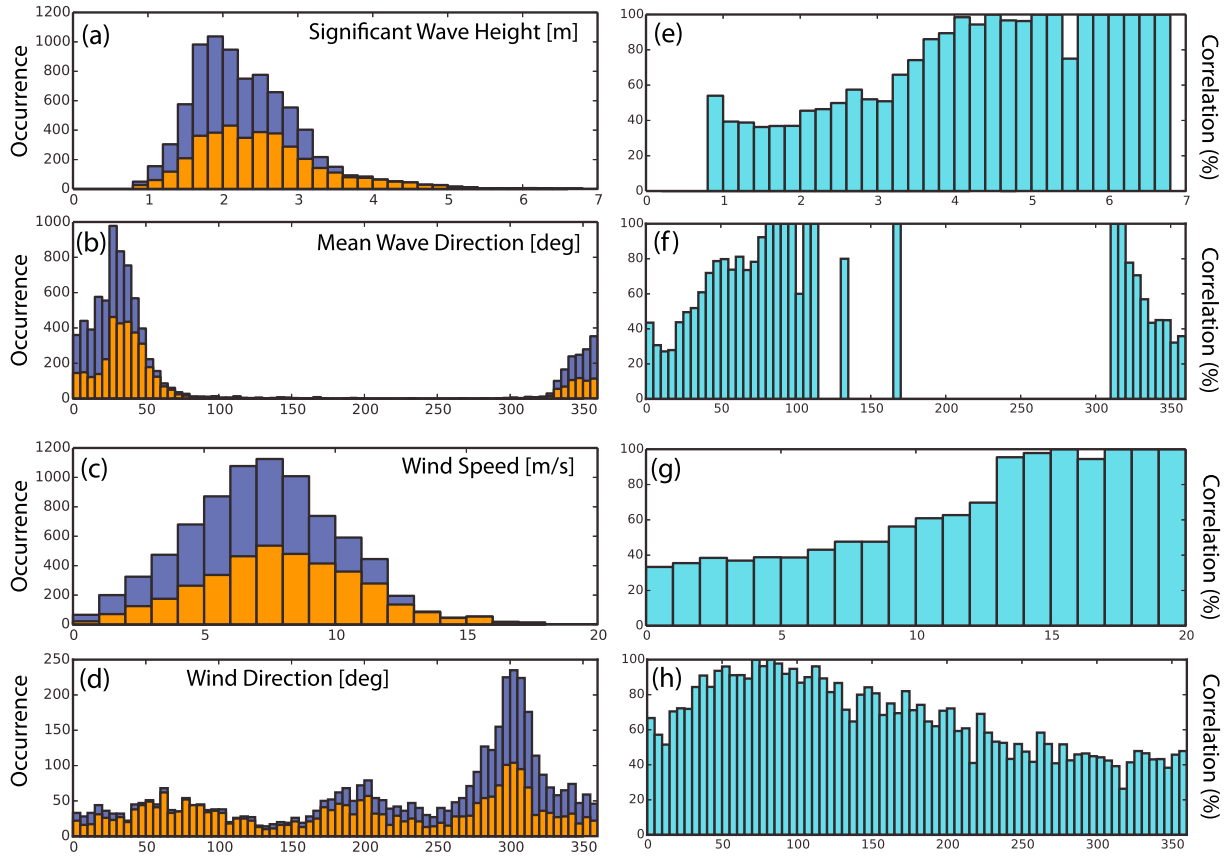

Figure 9. Parameters extracted from the ocean hindcast model for sector 8 (Great Australian Bight) and frequency band 1, for the full year of 2011: (a) wave height, (b) mean wave direction, (c) wind strength, and (d) mean wind direction. Parameters are shown as a histogram for the complete year (violet) and for time intervals when corresponding dominant surface wave arrivals were observed (orange). (e–h) The correlation between the two histograms (violet and orange) is given in the right-hand column. Correlation for mean wave height is only plotted if at least 10 measurements for a given direction occur during the year. Results for wind direction are constrained to wind speeds higher than 7 m/s as lower wind speeds are unlikely to have any effect on the generation of surface waves in frequency band 1.

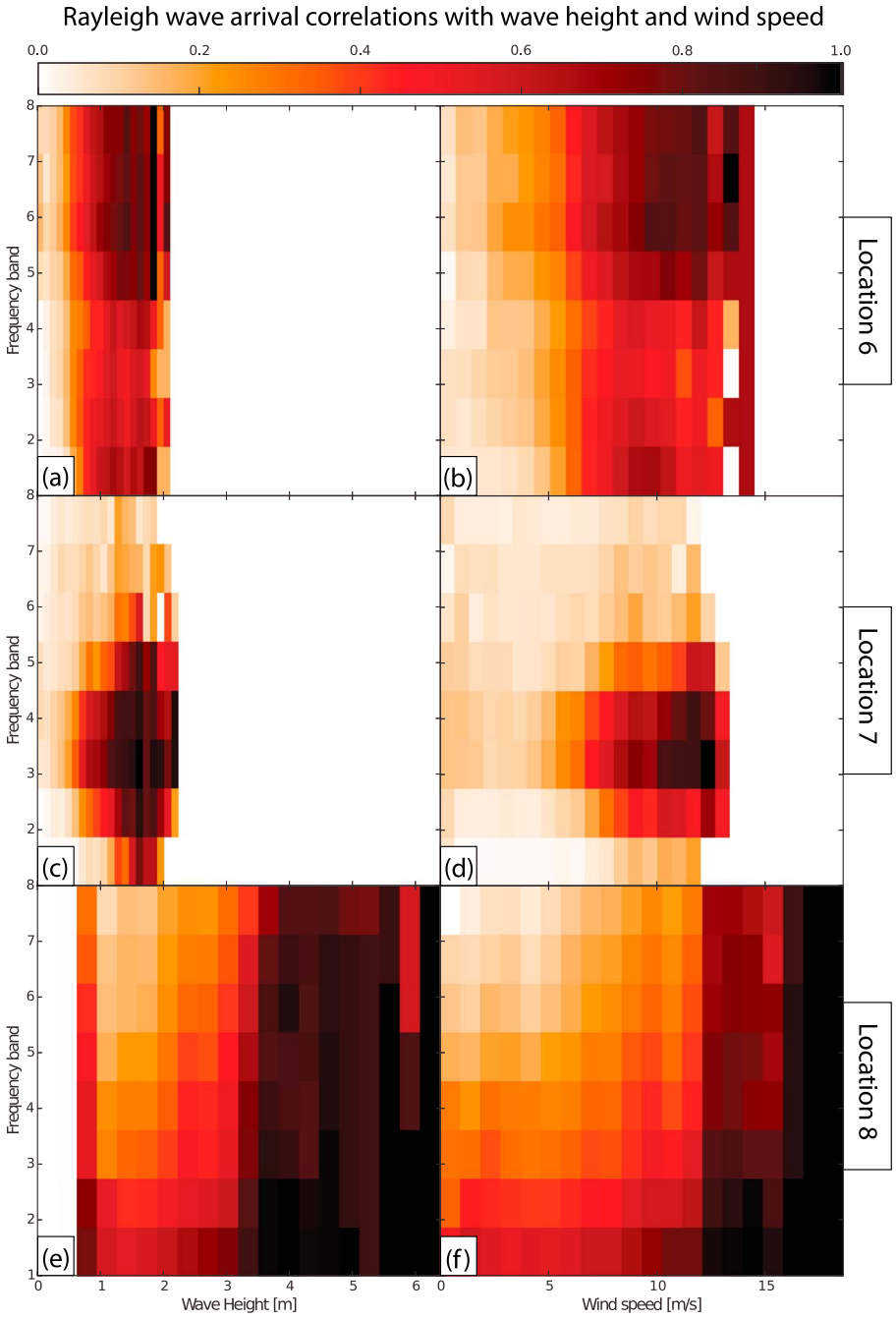

Figure 10. Frequency-dependent correlations between arrivals of Rayleigh waves and (left) wave height and (right) wind speed for locations (a and b) 6, (c and d) 7, and (e and f) 8.

between 0.038 and 0.5 Hz and 24 equally spaced directions ($\Delta = 15°$). Coastal reflections are not taken into account in this model.

We discretize the seismic arrivals into sectors (Figure 8a) that coincide with spatially concentrated surface wave back azimuths extracted from a histogram over the full period of the study. For each sector, we select a grid point of the ocean wave hindcast to represent the local wave and wind state. The location of the grid point is selected to be closest to the maximal arrival count of each sector and close to the coastline. For each surface wave arrival from a sector *n*, we record the ocean and wind state at grid point *n* during the same time period to investigate correlations between seismic arrivals and the ocean and wind state. We acknowledge

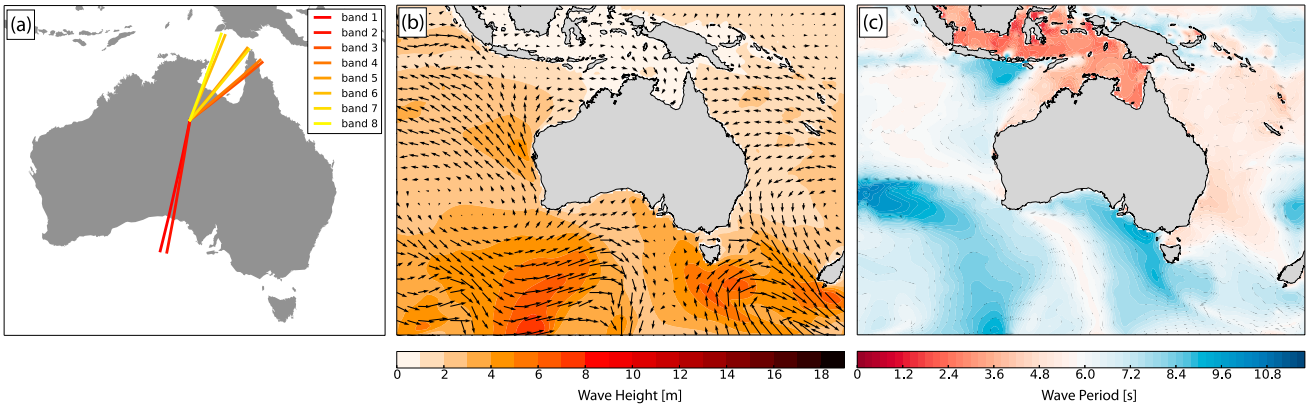

Figure 11. (a) Dominant surface wave arrivals for eight different frequency bands observed in the same 1 h record at WRA for the date 01 January 2010, 03:00:00 UTC. The estimated back azimuth is strongly dependent on the frequency band. The length of the raypath is arbitrary. (b) Wave height and (c) wave period for the same date as predicted by the ocean hindcast. The arrows in Figure 11b display the wind direction, and the length of the arrow corresponds to wind speed.

that wave height is not, in general, the dominant factor for the generation of microseisms [*Obrebski et al.*, 2012], which arise due to the interaction of opposing wave trains; however, within the areas shown in section 3, where surface waves are consistently generated, the scenario of opposing wave trains is realized and wave height is a good additional correlation parameter.

The results for sector 8 and band 1 are summarized in Figure 9. We find a strong correlation between seismic arrivals and ocean wave height and wind speed and a slightly preferred mean wave and wind direction. For a complete picture, we extend this analysis to all eight frequency bands and show wave height and wind speed correlations for sectors 6, 7, and 8 (Figure 10). These three sectors show unique correlation patterns with varying frequency. Sector 6 (north) shows the highest correlation for band 8 and reduced correlation toward band 1, sector 8 (south) shows the inverse effect with frequency, and sector 7 shows the highest correlation in band 3. The important information in these graphs is that for location 6, which is sheltered from long-period ocean swells (>6 s), higher-frequency Rayleigh waves are more likely to be excited by smaller ocean waves or less strong wind speed in comparison to band 1. In order to generate Rayleigh waves from sector 6 and band 1, the wind speed and wave height have to be greater on average. The hindcast also shows the dominant wind and wave direction to be around 270°. As the northern ocean basin is sheltered from remote swells and dominated by east winds, the local wind sea is the driving mechanism for the generation of Rayleigh waves. For the exposed southern sector 8, long-period swell mostly originates from remote parts of the southern Indian Ocean, and seismic arrivals are only observed during times of strong winds and increased wave heights for band 8. The strong source at sector 7 in band 3 cannot be explained by the hindcast data alone. WRA is recording Rayleigh waves from sector 7 mainly for wind and swell directions between 250 and 330°. The generation of Rayleigh waves is likely to be connected with the location of Mornington Island (Figure 8b), and resonance effects between the coastline and Mornington Island may be the cause of the strong source in band 3.

The above results represent a yearly average for the seismic and ocean hindcast data. To highlight the diversity of the secondary microseism wavefield, we display the arrival direction of the dominant surface wave in each frequency band for a single hour (Figure 11a). We find the two lowest-frequency bands pointing southward, while higher-frequency bands show arrivals from the northeast. We further present the ocean wave height (Figure 11b) and dominant wave period (Figure 11c) for the same time frame (1 January 2010, 03:00 UTC). For the Great Australian Bight, we find a swell height around 3 m and period of 7–8 s. This fits well with the seismic observations for the lower-frequency bands. To the northeast, we find a swell height below 1 m and periods below 4 s, which fits well with the observations in the higher-frequency bands and supports our previous conclusion that the wind sea is the main contributor to the generation of higher-frequency secondary microseisms. The average depth for the northeast sources is around 50–60 m and shows that Rayleigh waves are excited in shallow waters.

4.3. Seasonal Variations

To examine the seasonal patterns of surface waves at WRA, we sum all arrivals in all frequency bands for the whole time period of the study (Figure 12). The figure is normalized and shows a monthly average of

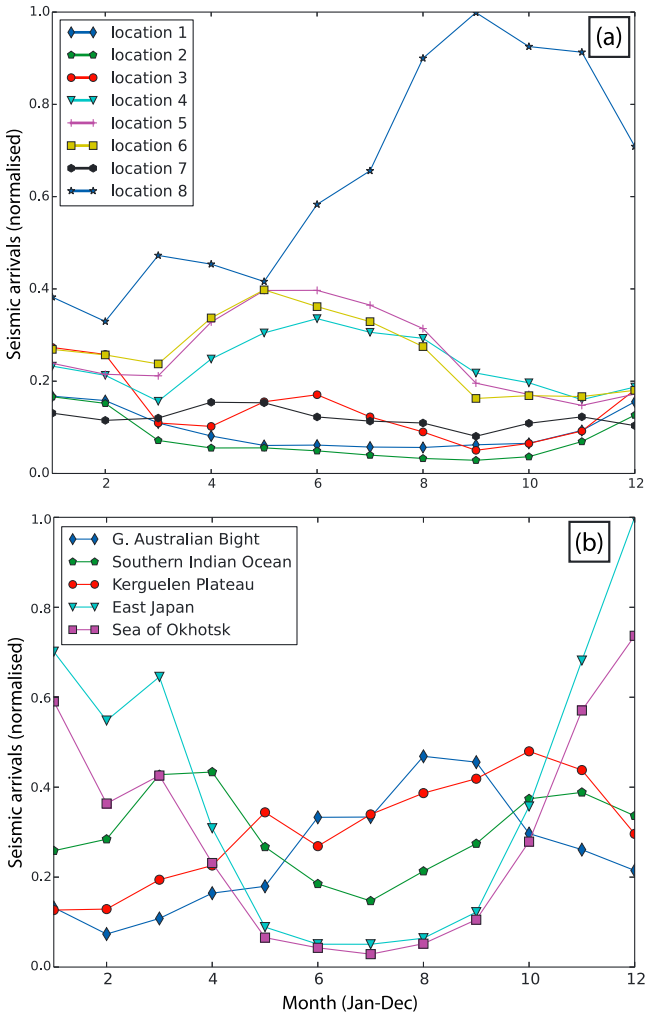

Figure 12. Seasonality shown as seismic arrival hit count (normalized) per month for (a) surface waves and (b) *P* waves. See Figure 8a for the match to geographic location for surface waves. *P* wave arrivals for the southern Indian Ocean are mostly those in the region south of Australia. The five strongest arrivals per evaluated hour were used for the computation of monthly averages.

each of the sources. We find the Great Australian Bight (sector 8; Figure 8a) to be the main contributor to microseism arrivals over the whole year, with a minimum of activity in February and a maximum in September. This can be explained by the fact that the Great Australian Bight is the closest southern coastline to WRA that receives major swells and the main swell direction has a frontal incident angle on the coastline, which would allow wave reflections over a large area. Sectors 4, 5, and 6 display similar activity with a maximum in June, while sectors 1, 2, and 3 display the inverse pattern with a maximum in January. Sector 7 remains relatively constant over the whole year, on average.

To examine the long-term stability of the seismic arrivals, we next evaluate each year separately. The data do not reveal any changing trend except for marginal variations, which can be explained by strong storm events. The seasonally dependent seismic arrival count also remains the same for each year and each frequency bin, which suggests that global swell and wind patterns remain approximately the same. The seasonality of body waves recorded at WRA has been discussed previously by *Reading et al.* [2014] and is in agreement with our present results for the Kerguelen Plateau and Sea of Okhotsk/east Japan region (Figure 12b). The Kerguelen Plateau shows its minimum in January and displays a slow rise in *P* wave generation that peaks in October. For the Sea of Okhotsk and east Japan we find a similar pattern, which peaks in December and displays its *P* wave minimum in July. The number of estimated *P* waves from the Great Australian Bight correlates well with the surface wave pattern from this location and peaks in the southern hemisphere winter months. This suggests that *P* waves are probably generated by coastal reflections as well, by the same swell systems that excite surface waves. The source in the southern Indian Ocean shows two peaks, in April and November, which are consistent with peaks in wind strength data in this region.

5. Discussion

In this section we discuss the possible mechanisms for the conversion of R_g-to-L_g waves, followed by the generation region of surface waves. Further, we discuss the correlations with an ocean wave hindcast, and swell and wind parameters, in more detail. The results in section 3.1.1 show an increase in the relative abundance of L_g with respect to R_g, with increasing frequency. Although most of the microseism energy is present in the form of Rayleigh waves [*Lacoss et al.*, 1969], a previous study on IMS arrays and short-period microseisms has shown L_g waves to be the dominant contributor in the frequency range of 0.5–4 Hz

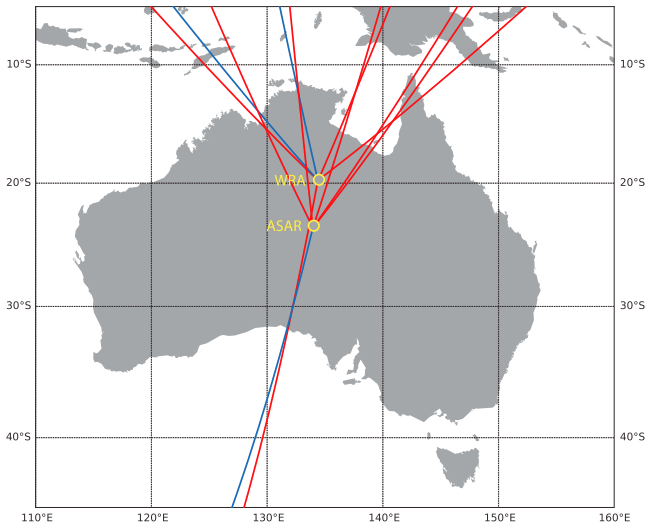

Figure 13. Triangulation of surface waves from ASAR and WRA. The red raypaths denote R_g waves, while the blue raypaths denote L_g waves.

[*Koper et al.*, 2010]. As L_g waves are unlikely to propagate in the oceanic crust [*Zhang and Lay*, 1995], *Koper et al.* [2010] argued that irregular morphology of coastlines is a possible cause for L_g excitation.

For explosive seismic sources it has been suggested that L_g waves are generated by near-source scattering of R_g waves [*Patton and Taylor*, 1995; *Gupta et al.*, 1997]. The conversion mechanism/transfer function was found to be frequency and source-depth dependent [*Myers et al.*, 1999]. Additionally, a numerical study was performed to investigate the influence of a rugged free surface on seismic phase conversion in the frequency range of 1–4 Hz [*He et al.*, 2008]. It was found that a considerable amount of R_g energy is scattered into L_g waves for low frequencies (1 Hz). In our study, we find the back azimuth of impinging R_g and L_g arrivals to be similar (Figure 2), which favors an R_g-to-L_g conversion for which irregular morphology of coastlines or rugged surface scattering are potential candidates.

The analysis of surface wave microseism locations shows a stationary behavior with respect to frequency over the full duration of the study. This supports our assumption that coastline reflections are the main contributors to the generation of surface waves around Australia, as coastline geometry, bathymetry, and storm tracks remain constant over two decades. We find small variations between the results estimated before and after 2000. Since all post-2000 results show a similar behavior, the small differences in the arrival patterns are likely to be connected to different seismic instruments and the absence of four stations in WRA prior to 1999. Although we find concentrated source regions for surface waves, their actual generation distance from the coasts is unknown. Observing the arrivals from the north (Figures 6a and 6b) and relating them to the amplitude maps (Figures 6c and 6d), we do not find any relation that can explain the strong geographical concentration of source regions. The main factor for this spatial concentration should therefore be the coastline geometry, which supports the idea of nearshore generation regions.

It is possible in surface wave microseism analysis to use multiple arrays to infer the distance to the source region via triangulation [*Cessaro and Chan*, 1989; *Cessaro*, 1994; *Friedrich et al.*, 1998]. We explored this possibility by analyzing 6 years of data from the Alice Springs Array (ASAR; for station configuration, see Figure S1a), which is located about 410 km south of WRA. ASAR has smaller interstation spacing and aperture compared to WRA, and so its array response is optimal at slightly higher frequencies. However, we can compare the back azimuths of surface wave arrivals for these two arrays because our results have shown that the back azimuth of surface waves remains relatively constant with frequency. The ASAR results confirm some locations seen by WRA (Figure 13). For arrivals from the north and south, for which ASAR and WRA are aligned with the source direction, triangulation does not yield meaningful information on the source distance from the shorelines; however, for arrivals from the northwest we find the source location via triangulation to be immediately offshore. We conclude that the generation of surface wave microseisms is mainly driven by coastal reflections, aided by bathymetry effects. The slope-coastline configuration does not seem to play an important role in the generation of short-period surface waves. The figure also shows that R_g and L_g waves are observed for the same source region by the two arrays. This finding strengthens the idea of an R_g-to-L_g conversion.

For weaker surface wave arrivals we observe a small shift in back azimuth with varying frequency (Figure 2). A possible explanation is a frequency-dependent coastal reflection coefficient, hence a varying dominant frequency for different spatial points. For the sources in the northwest, 280–330°, the mean swell direction is from the southern Indian Ocean, and with increasing frequency we see these sources shifting toward a

lower back azimuth (south). We see the same effect for the surface wave sources in the northeast, 10–55°. The mean swell direction for the northeast basin is from the east to west, and for increasing frequency the generation location is shifting toward a higher back azimuth, i.e., east toward the swell direction.

We find both R_g and L_g arrivals from each source region with the exception of the region around a back azimuth of 50°. The L_g signal is absent from the dominant summary plot (Figure 2b) and starts showing a weak presence for tertiary L_g arrivals (Figure 2f). We performed a correlation analysis between the ocean hindcast and the recorded seismic arrivals to investigate the Coral Sea as a possible source generation location, as the reentry of the L_g phase might be attenuated due to the crossing of the oceanic lithosphere. The results show correlation coefficients below 0.20 and a random distribution with wave height and wind speed between seismic arrivals and the Coral Sea hindcast parameters. Because all other sources show a strong correlation, we conclude that the seismic signal does not originate from the Coral Sea but from a closer location. Therefore, the correlation of Rayleigh waves with the ocean hindcast shows great utility for the identification of the generation region in the case of a raypath crossing multiple coastlines.

Further insight can be gained by observing the distribution and correlation between Rayleigh wave arrivals, mean wave direction (Figures 9b and 9f), and wind direction (Figures 9d and 9h) for sector 8 and band 1. The majority of the swell is generated in the southern Indian Ocean and reaches sector 8 around 25°. As can be seen from the mean wave direction correlation, certain wave directions are more likely to generate Rayleigh waves that can be measured at WRA. We observe a local minimum for the correlation coefficient around 10°–15° and increasing toward 290° or 110°. A possible explanation is that the reflection coefficient of coastlines is swell direction dependent and can promote suitable conditions for the generation of secondary microseisms. For swell directions that face away from the coastlines, it is likely that two swell/wind sea trains are responsible, which would explain the high correlation and the rarity of the event at the southern Australian coast. The wind direction correlation shows a smoother distribution and a trend toward onshore wind. The trend toward onshore wind becomes stronger with increasing frequency, and other wind directions show a less correlated behavior. This is in agreement with the conclusion that higher-frequency arrivals are generated by local wind sea [*Zhang et al*., 2009].

6. Conclusion

We have evaluated two decades of ambient seismic noise in a frequency-dependent analysis of vertical component data from the Warramunga Array in central Australia. For an accurate interpretation of the incoming signals, we made use of the IAS Capon algorithm followed by a mislocation vector analysis to reduce the slowness and back azimuth bias in *P* waves attributed to 3-D variations in geology near the array.

For surface waves, we find preferred back azimuthal directions except from the southeastern region, which remains arrival free for the entire time period and frequency band of our study. Lower-frequency bands ($<$0.55 Hz) are dominated by R_g arrivals from a range of distances, while higher-frequency bands ($>$0.55 Hz) show a transition to L_g arrivals and a preference for nearby coastlines, except for the Great Australian Bight. Weaker arrivals show new spatially concentrated generation regions and extend the frequency range of previously observed microseism sources at WRA [*Reading et al*., 2014]. R_g and L_g waves display similar back azimuths, which suggest an R_g-to-L_g conversion mechanism, possibly similar to the generation of L_g from nuclear explosions [*Patton and Taylor*, 1995; *Gupta et al*., 1997]. Irregular coastline morphology and the scattering on a free rugged surface were identified as possible conversion mechanisms. Surface waves can show a back azimuth drift with respect to frequency, which is most likely connected to bathymetry effects. Triangulation with the Alice Springs Array (ASAR) and the strong spatial concentration of the arrivals suggest the generation regions of surface waves to be close to coastlines.

P wave microseism locations are found to be frequency dependent. For the lower-frequency bands (0.325–0.475 Hz), we find the dominant arrivals to originate from deep waters in the southern Indian Ocean and north of Japan (Sea of Okhotsk), showing good correlation with regions with strong amplitude coefficients. For higher-frequency bands (0.525–0.725 Hz), we see a migration of body wave arrivals toward shallower regions: the Great Australian Bight, the Kerguelen Plateau, in the South Pacific Ocean south of New Zealand, and the east coast of Japan. In higher-frequency bands, these regions are less correlated with regions with strong amplitude coefficients, and the presence of coastal boundaries

outweighs the importance of bathymetry effects. We further show that weaker body wave arrivals are not contaminated by earthquake arrivals and, in fact, reveal new *P* wave source regions. In our study, weaker arrivals revealed increased *P* wave activity from the northeast Coral Sea, the eastern coastlines of the Philippines, and Taiwan.

We compared our microseism observations to a WAVEWATCH III hindcast and observed strong correlations between microseismic activity and ocean wave height and wind speed for regions with consistent surface wave sources. We further observed a preferred, onshore, wind direction for the generation of surface waves. The wind direction is found to be increasingly important for higher frequencies, as the local wind sea is the main generator of surface waves observed at WRA. The hindcast can be used to distinguish between surface wave generation regions in the case of a raypath crossing two or more coastlines.

Acknowledgments
We acknowledge data access through the IRIS DMC archive, the Australian National University, and the ISC. We thank the Tasmanian Partnership for Advanced Computing, which enabled the access to its HPC Facilities. The research was funded by the Australian Research Council (DP150101005). M.G. is supported through a Tasmanian Government Research Scholarship. L.G. acknowledges support from a Lamont-Doherty Earth Observatory Postdoctoral Fellowship and the Brinson Foundation. K.D.K. and R.B. acknowledge support from NSF-EarthScope under award EAR-091558. IAS Capon code and beam-forming results for the whole span of two decades are freely available in the NetCDF4 file format and may be obtained by contacting the University of Tasmania authors.

References

Ardhuin, F., and A. Roland (2012), Coastal wave reflection, directional spread, and seismoacoustic noise sources, *J. Geophys. Res.*, *117*, C00J20, doi:10.1029/2011JC007832.

Ardhuin, F., L. Gualtieri, and E. Stutzmann (2015), How ocean waves rock the Earth: Two mechanisms explain microseisms with periods 3 to 300 s, *Geophys. Res. Lett.*, *42*, 765–772, doi:10.1002/2014GL062782.1.

Aster, R. C., D. E. McNamara, and P. D. Bromirski (2010), Global trends in extremal microseism intensity, *Geophys. Res. Lett.*, *37*, L14303, doi:10.1029/2010GL043472.

Behr, Y., J. Townend, M. Bowen, L. Carter, R. Gorman, L. Brooks, and S. Bannister (2013), Source directionality of ambient seismic noise inferred from three-component beamforming, *J. Geophys. Res. Solid Earth*, *118*, 240–248, doi:10.1029/2012JB009382.

Berger, J., P. Davis, and G. Ekström (2004), Ambient Earth noise: A survey of the global seismographic network, *J. Geophys. Res.*, *109*, B11307, doi:10.1029/2004JB003408.

Beucler, E., A. Mocquet, M. Schimmel, S. Chevrot, O. Quillard, J. Vergne, and M. Sylvander (2015), Observation of deep water microseisms in the North Atlantic Ocean using tide modulations, *Geophys. Res. Lett.*, *42*, 316–322, doi:10.1002/2014GL062347.

Bokelmann, G. (1995), Azimuth and slowness deviations from the GERESS regional array, *Bull. Seismol. Soc. Am.*, *85*(5), 1456–1463.

Bondár, I., R. North, and G. Beall (1999), Teleseismic slowness-azimuth station corrections for the International Monitoring System seismic network, *Bull. Seismol. Soc. Am.*, *89*(4), 989–1003.

Boué, P., P. Poli, M. Campillo, H. Pedersen, X. Briand, and P. Roux (2013), Teleseismic correlations of ambient seismic noise for deep global imaging of the Earth, *Geophys. J. Int.*, *194*(2), 844–848, doi:10.1093/gji/ggt160.

Bromirski, P. D., R. A. Stephen, and P. Gerstoft (2013), Are deep-ocean-generated surface-wave microseisms observed on land?, *J. Geophys. Res. Solid Earth*, *118*, 3610–3629, doi:10.1002/jgrb.50268.

Cessaro, R. K. (1994), Sources of primary and secondary microseisms, *Bull. Seismol. Soc. Am.*, *84*(1), 142–148.

Cessaro, R. K., and W. W. Chan (1989), Wide-angle triangulation array study of simultaneous primary microseism sources, *J. Geophys. Res.*, *94*, 15,555–15,563, doi:10.1029/JB094iB11p15555.

Chevrot, S., M. Sylvander, S. Benahmed, C. Ponsolles, J. M. Lefèvre, and D. Paradis (2007), Source locations of secondary microseisms in western Europe: Evidence for both coastal and pelagic sources, *J. Geophys. Res.*, *112*, B11301, doi:10.1029/2007JB005059.

Deacon, G. E. R. (1947), Relations between sea waves and microseisms, *Nature*, *160*, 419–421, doi:10.1038/160419a0.

Durrant, T., M. Hemer, C. Trenham, and D. Greenslade (2013a), CAWCR wave hindcast 1979–2010, v5., *CSIRO. Data Collection*., doi:10.4225/08/523168703DCC5.

Durrant, T., M. Hemer, C. Trenham, and D. Greenslade (2013b), CAWCR wave hindcast extension Jan 2011-May 2013, v2., *CSIRO. Data Collection*., doi:10.4225/08/52817E2858340.

Essen, H.-H. (2003), On the generation of secondary microseisms observed in northern and central Europe, *J. Geophys. Res.*, *108*(B10), 2506, doi:10.1029/2002JB002338.

Friedrich, A., K. Klinge, and F. Krüger (1998), Ocean-generated microseismic noise located with the Graefenberg array, *J. Seismol.*, *2*(1), 47–64.

Gal, M., A. M. Reading, S. P. Ellingsen, K. D. Koper, S. J. Gibbons, and S. P. Näsholm (2014), Improved implementation of the fk and Capon methods for array analysis of seismic noise, *Geophys. J. Int.*, *198*(2), 1045–1054, doi:10.1093/gji/ggu183.

Gerstoft, P., P. M. Shearer, N. Harmon, and J. Zhang (2008), Global *P*, *PP*, and *PKP* wave microseisms observed from distant storms, *Geophys. Res. Lett.*, *35*, 1–6, doi:10.1029/2008GL036111.

Gualtieri, L., E. Stutzmann, Y. Capdeville, F. Ardhuin, M. Schimmel, A. Mangeney, and A. Morelli (2013), Modelling secondary microseismic noise by normal mode summation, *Geophys. J. Int.*, *193*(3), 1732–1745, doi:10.1093/gji/ggt090.

Gualtieri, L., E. Stutzmann, V. Farra, Y. Capdeville, M. Schimmel, F. Ardhuin, and A. Morelli (2014), Modelling the ocean site effect on seismic noise body waves, *Geophys. J. Int.*, *197*(2), 1096–1106, doi:10.1093/gji/ggu042.

Gupta, I., T. Zhang, and R. Wagner (1997), Low-Frequency L_g from NTS and Kazakh nuclear explosions—Observations and interpretation, *Bull. Seismol. Soc. Am.*, *87*(5), 1115–1125.

Gutenberg, B. (1936), On microseisms, *Bull. Seismol. Soc. Am.*, *26*(2), 111–117.

Hasselmann, K. (1963), A statistical analysis of the generation of microseisms, *Rev. Geophys.*, *1*(2), 177–210, doi:10.1029/RG001i002p00177.

He, Y., X.-B. Xie, and T. Lay (2008), Explosion-source energy partitioning and L_g-wave excitation: Contributions of free-surface scattering, *Bull. Seismol. Soc. Am.*, *98*(2), 778–792, doi:10.1785/0120070119.

International Seismological Centre (2012), Online Bulletin, *Int. Seis. Cent.*, *Thatcham*, *United Kingdom*. [Available at http://www.isc.ac.uk.]

Jacobeit, E., C. Thomas, and F. Vernon (2013), Influence of station topography and Moho depth on the mislocation vectors for the Kyrgyz Broadband Seismic Network (KNET), *Geophys. J. Int.*, *193*(2), 949–959, doi:10.1093/gji/ggt014.

Kedar, S., M. Longuet-Higgins, F. Webb, N. Graham, R. Clayton, and C. Jones (2008), The origin of deep ocean microseisms in the North Atlantic Ocean, *Proc. R. Soc. London, Ser. A Math. Phys. Eng. Sci.*, *464*(2091), 777–793, doi:10.1098/rspa.2007.0277.

Kennett, B. L. N., E. R. Engdahl, and R. Buland (1995), Constraints on seismic velocities in the Earth from traveltimes, *Geophys. J. Int.*, *122*(1), 108–124, doi:10.1111/j.1365-246X.1995.tb03540.x.

Koper, K. D., B. de Foy, and H. Benz (2009), Composition and variation of noise recorded at the Yellowknife Seismic Array, 1991–2007, *J. Geophys. Res.*, *114*, 1–13, doi:10.1029/2009JB006307.

Koper, K. D., K. Seats, and H. Benz (2010), On the composition of Earth's short-period seismic noise field, *Bull. Seismol. Soc. Am.*, *100*(2), 606–617, doi:10.1785/0120090120.

Lacoss, R., E. Kelly, and M. Toksöz (1969), Estimation of seismic noise structure using arrays, *Geophysics*, *34*(1), 21–38.

Longuet-Higgins, M. (1950), A theory of the origin of microseisms, *Philos. Trans. R. Soc. London Ser. A. Math. Phys. Sci.*, *243*(857), 1–35.

Manchee, E. B., and D. H. Weichert (1968), Epicentral uncertainties and detection probabilities for the Yellowknife Seismic Array data, *Bull. Seismol. Soc. Am.*, *58*, 1359–1377.

Myers, S., W. Walter, K. Mayeda, and L. Glenn (1999), Observations in support of R_g scattering as a source for explosion *S* waves: Regional and local recordings of the 1997 Kazakhstan depth of burial experiment, *Bull. Seismol. Soc. Am.*, *89*(2), 544–549.

Nishida, K., H. Kawakatsu, Y. Fukao, and K. Obara (2008), Background Love and Rayleigh waves simultaneously generated at the Pacific Ocean floors, *Geophys. Res. Lett.*, *35*, L16307, doi:10.1029/2008GL034754.

Obrebski, M. J., F. Ardhuin, E. Stutzmann, and M. Schimmel (2012), How moderate sea states can generate loud seismic noise in the deep ocean, *Geophys. Res. Lett.*, *39*, L11601, doi:10.1029/2012GL051896.

Patton, H., and S. Taylor (1995), Analysis of L_g spectral ratios from NTS explosions: Implications for the source mechanisms of spall and the generation of L_g waves, *Bull. Seismol. Soc. Am.*, *85*(1), 220–236.

Reading, A. M., K. D. Koper, M. Gal, L. S. Graham, H. Tkalčić, and M. A. Hemer (2014), Dominant seismic noise sources in the Southern Ocean and West Pacific, 2000–2012, recorded at the Warramunga Seismic Array, Australia, *Geophys. Res. Lett.*, *41*, 3455–3463, doi:10.1002/2014GL060073.

Schulte-Pelkum, V., P. S. Earle, and F. L. Vernon (2004), Strong directivity of ocean-generated seismic noise, *Geochem. Geophys. Geosyst.*, *5*, Q03004, doi:10.1029/2003GC000520.

Schweitzer, J. (2001), Slowness corrections—One way to improve IDC products, *Pure Appl. Geophys.*, *158*, 375–396.

Stutzmann, E., G. Roult, and L. Astiz (2000), GEOSCOPE station noise levels, *Bull. Seismol. Soc. Am.*, *90*(3), 690–701.

Traer, J., P. Gerstoft, P. D. Bromirski, and P. M. Shearer (2012), Microseisms and hum from ocean surface gravity waves, *J. Geophys. Res.*, *117*, B11307, doi:10.1029/2012JB009550.

Wiechert, E. (1904), Verhandlungen der zweiten internationalen Seismologischen Konferenz [in German], *Gerlands Beitr. Geophys.*, *2*, 41–43.

Zhang, J., P. Gerstoft, and P. M. Shearer (2009), High-frequency *P*-wave seismic noise driven by ocean winds, *Geophys. Res. Lett.*, *36*, L09302, doi:10.1029/2009GL037761.

Zhang, T., and T. Lay (1995), Why the L_g phase does not traverse oceanic crust, *Bull. Seismol. Soc. Am.*, *85*(6), 1665–1678.